

Dislocation-induced stop-and-go kinetics of interfacial transformations

<https://doi.org/10.1038/s41586-022-04880-1>

Received: 21 October 2020

Accepted: 19 May 2022

Published online: 27 July 2022

 Check for updates

Xianhu Sun^{1,4}, Dongxiang Wu^{1,4}, Lianfeng Zou¹, Stephen D. House², Xiaobo Chen¹, Meng Li², Dmitri N. Zakharov³, Judith C. Yang² & Guangwen Zhou^{1✉}

Most engineering materials are based on multiphase microstructures produced either through the control of phase equilibria or by the fabrication of different materials as in thin-film processing. In both processes, the microstructure relaxes towards equilibrium by mismatch dislocations (or geometric misfit dislocations) across the heterophase interfaces^{1–5}. Despite their ubiquitous presence, directly probing the dynamic action of mismatch dislocations has been unachievable owing to their buried nature. Here, using the interfacial transformation of copper oxide to copper as an example, we demonstrate the role of mismatch dislocations in modulating oxide-to-metal interfacial transformations in an intermittent manner, by which the lateral flow of interfacial ledges is pinned at the core of mismatch dislocations until the dislocation climbs to the new oxide/metal interface location. Together with atomistic calculations, we identify that the pinning effect is associated with the non-local transport of metal atoms to fill vacancies at the dislocation core. These results provide mechanistic insight into solid–solid interfacial transformations and have substantial implications for utilizing structural defects at buried interfaces to modulate mass transport and transformation kinetics.

Fundamental understanding of mismatch dislocations and their dynamic coupling to phase transformations has been a long-standing topic of study^{6–18}. Transmission electron microscopy (TEM) has demonstrated its versatility and atomic-scale precision in elucidating the location and configuration of static dislocations^{7,10,18–22}. TEM has been used to observe dislocation motion during deformation^{13,23–25}. However, directly probing the dynamic action of mismatch dislocations during phase transformations is challenging because it requires a capability not only to atomically capture the fast evolution of interfaces but also to apply stimuli to drive the interface transformation.

Here we report direct visualization of the dynamic action of mismatch dislocations during an interface transformation. This is performed with the use of in situ environmental TEM to flow hydrogen (H₂) gas in the sample area to activate the copper oxide (Cu₂O)/copper (Cu) interface reaction while simultaneously resolving the Cu₂O → Cu interface transformation by high-resolution TEM (HRTEM) imaging. Our in situ TEM experiments (Supplementary Fig. 1) include the in-place Cu₂O/Cu interface formation through oxidizing Cu in oxygen (O₂), followed by switching to H₂, which results in the reduction of Cu₂O to Cu at the Cu₂O/Cu interface.

Figure 1a shows a typical HRTEM image of a Cu₂O(110)/Cu(110) interface formed at a partial pressure of oxygen (P_{O_2}) = 0.67 Pa and a temperature T = 623 K (Supplementary Figs. 2 and 3). The Cu₂O/Cu interface location is marked by the green dashed line in Fig. 1a and four mismatch dislocations are identified, showing both the 7 × 6 and 8 × 7 coincidence-site-lattice (CSL) configurations in which 6 (or 7) Cu

spacings in Cu₂O match 7 (or 8) Cu spacings in the Cu substrate. The large natural lattice misfit (about 14.5%) between Cu and Cu₂O (Supplementary Text 1) makes the formation of a coherent interface energetically unfavourable, thereby resulting in an array of dislocations to release the misfit strain (Supplementary Text 1). This is confirmed by the geometrical phase analysis (GPA) of the HRTEM image, which shows concentrated strains around the dislocation core (Fig. 1b and Supplementary Tables 1 and 2). As shown later from our in situ TEM observations, 8 × 7 (and 6 × 5) segments appear transiently and transform to the more stable 7 × 6 CSL upon the Cu₂O → Cu interfacial transformation. Figure 1c is a zoom-in HRTEM image of a typical mismatch dislocation, showing a Burgers vector of $\mathbf{b} = \frac{1}{2}[\bar{1}10]$. This is further confirmed by HRTEM image simulations (Fig. 1d) using the density-functional-theory (DFT) optimized Cu₂O(110)/Cu(110) interface structure (Fig. 1e, Supplementary Texts 2 and 3, and Supplementary Figs. 4 and 5) and by high-angle annular dark-field (HAADF) imaging (Fig. 1f).

The Cu₂O/Cu interfaces formed from the in situ oxidation serve as an ideal platform to visualize the dynamic action of mismatch dislocations by switching the atmosphere from an O₂ to a H₂ gas flow that induces the reduction of Cu₂O to Cu. Figure 2a–d shows in situ HRTEM images of the Cu₂O → Cu transformation along the Cu₂O(110)/Cu(110) interface for a large Cu₂O island, where only the corner region is imaged. As indicated by yellow dashed lines in Fig. 2a–d, the Cu₂O/Cu interface is initially flat and is observed to migrate towards the Cu₂O side as the Cu₂O is transformed to metallic Cu along the Cu₂O/Cu interface. The interface is measured to migrate by about 1.8 nm towards the Cu₂O side

¹Department of Mechanical Engineering and Materials Science and Engineering Program, State University of New York at Binghamton, Binghamton, NY, USA. ²Department of Chemical and Petroleum Engineering, University of Pittsburgh, Pittsburgh, PA, USA. ³Center for Functional Nanomaterials, Brookhaven National Laboratory, Upton, NY, USA. ⁴These authors contributed equally: Xianhu Sun, Dongxiang Wu. ✉e-mail: gzhou@binghamton.edu

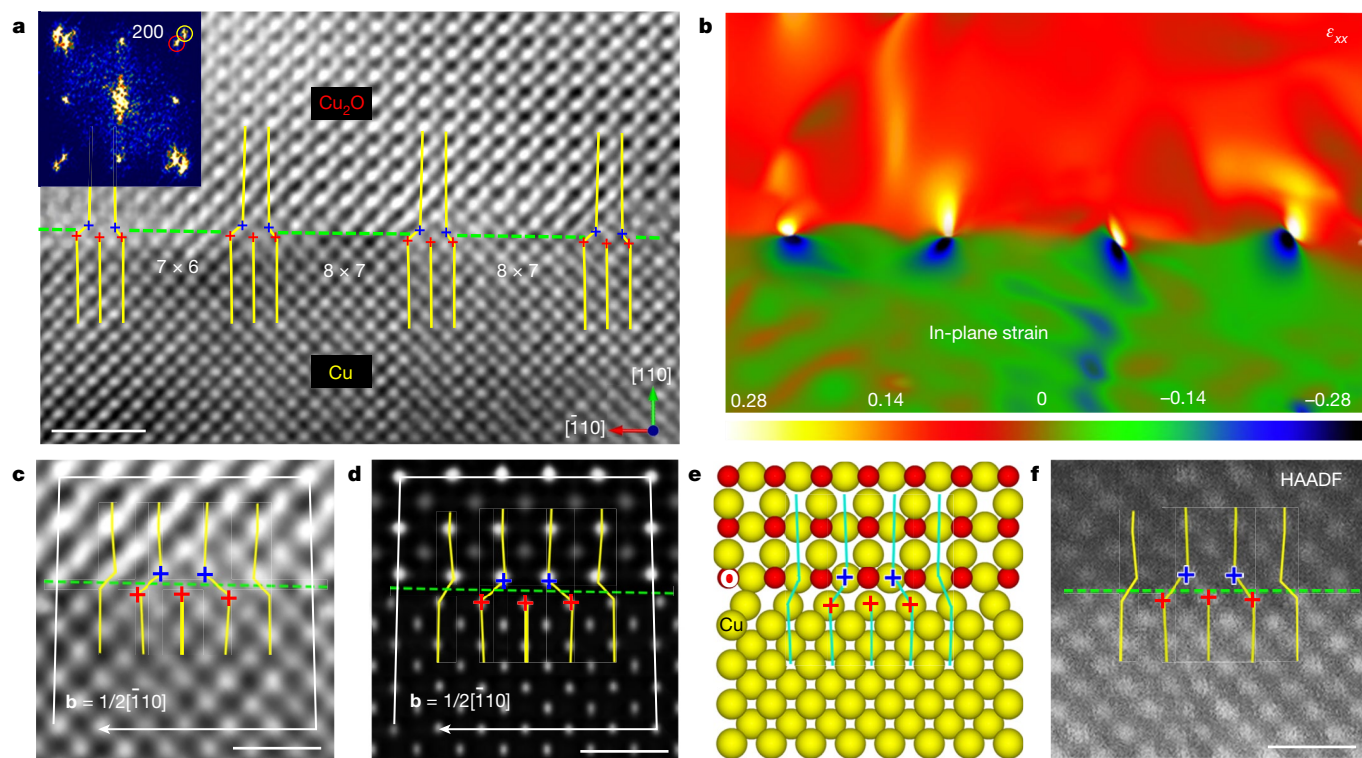


Fig. 1 | Formation of mismatch dislocations at the Cu₂O/Cu interface.

a, HRTEM image of a Cu₂O/Cu interface formed by in situ oxidation of a Cu(110) facet at $p_{\text{O}_2} = 0.67$ Pa and $T = 623$ K. The core regions of four mismatch dislocations along the Cu₂O/Cu interface (green dashed line) are marked with crosses. Inset: diffractogram of the HRTEM image. The yellow and red circles mark the (200) spots of Cu and Cu₂O, respectively. **b**, In-plane strain map (ϵ_{xx})

obtained by GPA of the HRTEM image in **a**. **c**, **d**, Experimental (**c**) and simulated (**d**) HRTEM micrographs showing the dislocation core structure, where the Burgers circuits are marked by white lines. **e**, DFT relaxed Cu₂O(110)/Cu(110) interface structure used for HRTEM simulations in **d**. **f**, HAADF-STEM image of a typical mismatch dislocation. Scale bars, 1 nm (**a**) and 0.5 nm (**c**, **d**, **f**).

within a time elapse of 102 s. As indicated by the blue and red arrows in Fig. 2b,c, the Cu₂O → Cu transformation occurs via the lateral flow of atomic ledges along the Cu₂O/Cu interface. The epitaxial Cu₂O/Cu interface is maintained through the ledge-flow transformation. However, the in situ TEM observation shows a striking stop-and-go manner of the Cu₂O → Cu transformation, by which the lateral propagation of the Cu₂O/Cu interface ledges is regularly interrupted with short pauses that range from 2 s to 6 s, as shown in the distance–time plot (Fig. 2e) of the lateral propagation of ledges 1 and 2 marked in Fig. 2b,c. Meanwhile, the Cu₂O surface undergoes slight decay, as indicated by tracing the temporal evolution of the oxide surface in Fig. 2d (Supplementary Text 4).

The discrete interfacial transformation is also observed along the (100) interface. Figure 2f–i illustrates another example of the Cu₂O → Cu interfacial transformation, where the in situ TEM observation is made at a relatively low magnification to visualize the entire interface of a small Cu₂O island on Cu(100). The inset HRTEM image in Fig. 2f confirms the (100)-type interface. The Cu₂O → Cu transformation occurs via lateral ledge flow along the Cu₂O(100)/Cu(100) interface, as indicated by the arrows in Fig. 2f–i. Similarly, the transformation shows the stop-and-go movement of ledges with short pauses, as illustrated in the distance–time plot (Fig. 2j) of the lateral propagation of ledges 3 and 4 marked in Fig. 2f–i. The above in situ TEM observations also illustrate that the stop-and-go interfacial transformation is independent of the oxide island size. It is noted that electron-beam irradiation effects on the Cu₂O → Cu transformation are negligible (Supplementary Text 5).

Figure 3 shows that the stop-and-go interface transformation is regulated by mismatch dislocations. That is, the ledge flow pauses at the core of the dislocations and then, a few seconds later, resumes its lateral propagation. Figure 3a–e shows in situ HRTEM images of the intermittent flow of the interfacial ledges along the Cu₂O(110)/Cu(110) interface. Figure 3a

shows three mismatch dislocations with the 8 × 7 CSL matching, where the atomic columns around the dislocation cores are marked by red crosses to trace the exact location of the dislocations. As marked by the yellow arrow in Fig. 3b, a ledge enters the field of view from the right side. This results in a ledge-and-terrace interface, where the two terraces are separated by a double-atomic-height ledge (that is, $2d_{\text{Cu}(220)}$), as marked by the yellow dashed lines in Fig. 3b. Correspondingly, the lateral ledge flow results in the growth of two atomic layers of Cu(220) by consuming the Cu₂O lattice in front of the ledge. The ledge flow does not sweep across the Cu₂O/Cu interface unimpeded. Instead, the ledge propagation is regularly interrupted at the core of the dislocations, where the ledge is pinned for about 2–6 s (Fig. 3f) and then resumes its lateral migration. Upon the passage of the ledge, the dislocation core is observed to climb by two atomic layers to the upper terrace of the Cu₂O/Cu interface. This is followed by the lateral glide of the dislocation core by one lattice spacing, thereby transforming the 8 × 7 CSL to a 7 × 6 CSL (Fig. 3c–e).

This intermittent ledge flow is also observed atomically at the Cu₂O(100)/Cu(100) interface. Figure 3g shows four mismatch dislocations, separated by segments of the 6 × 5, 8 × 7 and 7 × 6 CSL matching. The Cu₂O/Cu interface has a ledge-and-terrace configuration, where the two terraces are separated by a monoatomic step (that is, $d_{\text{Cu}(200)}$), as marked by arrow 1 in Fig. 3g. This interfacial ledge sits right above the core of the mismatch dislocation. After about 2 s of dwelling on the dislocation core, the ledge is seen to propagate quickly towards the right side and then stay at the core location of the next dislocation (Fig. 3h). Meanwhile, another monoatomic ledge enters the field of view from the right side and sits right above the dislocation core (arrow 2 in Fig. 3h). After about 0.5 s of dwelling on the dislocation core, ledge 2 resumes its lateral propagation towards the left side and becomes pinned at the core of the adjacent dislocation (Fig. 3i). Ledge 1 is still

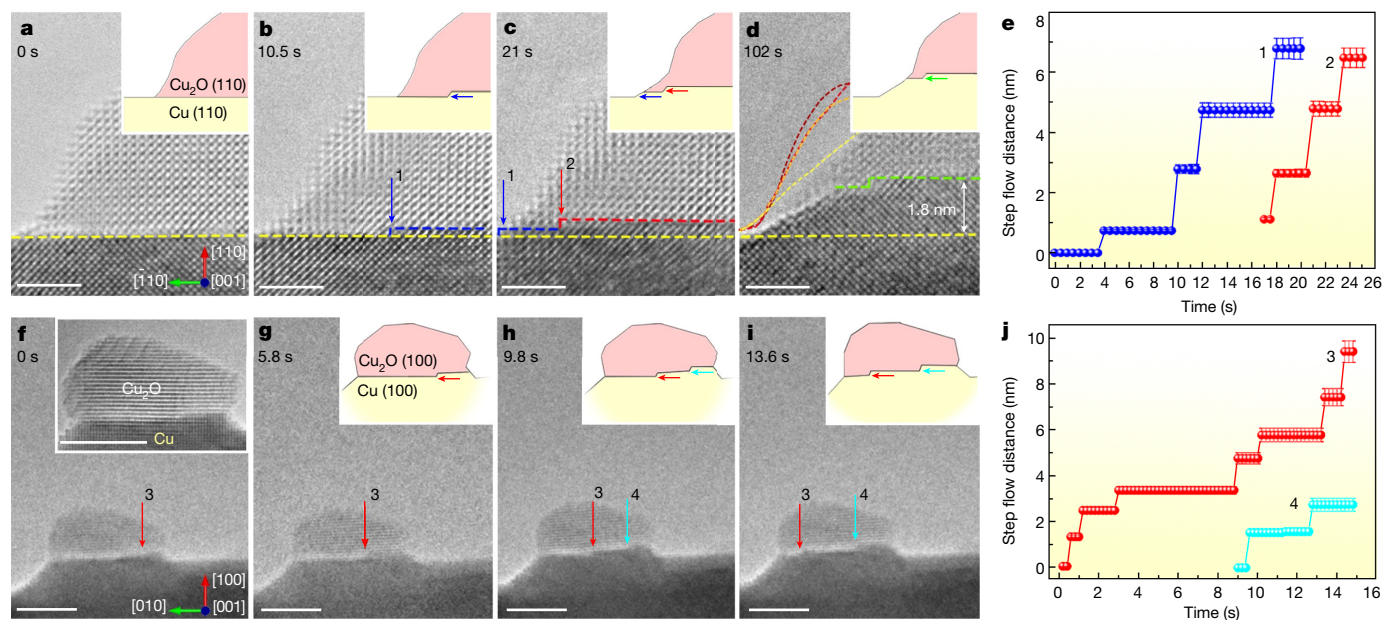


Fig. 2 | In situ TEM visualization of the stop-and-go ledge flow of the $\text{Cu}_2\text{O} \rightarrow \text{Cu}$ interfacial transformations at 623 K and 5.3 Pa of H_2 gas. **a–d**, Time-sequence HRTEM images showing the $\text{Cu}_2\text{O} \rightarrow \text{Cu}$ transformation along the $\text{Cu}_2\text{O}(110)/\text{Cu}(110)$ interface (Supplementary Video 1). Arrows 1 and 2 mark the $\text{Cu}_2\text{O}/\text{Cu}$ interfacial ledges. Between **c** and **d**, the e-beam was blanked for about 60 s to eliminate possible electron-beam effects on the interfacial transformation and then unblanked for TEM imaging. The dark red, red, orange and yellow dashed lines show the traces of the surface contour of the oxide at 0 s (**a**), 10.5 s (**b**), 21 s (**c**) and 102 s (**d**), respectively.

e, Distance–time plot measured from Supplementary Video 1 showing the lateral flow of ledges 1 and 2 in a stop-and-go manner. **f–i**, Time-sequence TEM images (Supplementary Video 2) showing the $\text{Cu}_2\text{O} \rightarrow \text{Cu}$ transformation along the $\text{Cu}_2\text{O}(100)/\text{Cu}(100)$ interface. Arrows 3 and 4 mark the lateral flow of the $\text{Cu}_2\text{O}/\text{Cu}$ interfacial ledges. **j**, Distance–time plot measured from Supplementary Video 2 showing the stop-and-go flow of ledges 3 and 4. Insets in **a–d** and **g–i** show schematically the ledge-flow transformation at the $\text{Cu}_2\text{O}/\text{Cu}$ interface. Inset in **f** is a zoom-in HRTEM image of the $\text{Cu}_2\text{O}/\text{Cu}$ interface region. Scale bars, 2 nm (**a–d**) and 5 nm (**f–i**).

pinned at the dislocation core during this time period. After another approximately 0.5 s of dwelling on the dislocation core, ledges 1 and 2 are observed to propagate towards each other, thereby resulting in the annihilation of the two interfacial ledges upon their meeting up (Fig. 3j). Same as the $\text{Cu}_2\text{O}(110)/\text{Cu}(110)$ interface, the stop-and-go flow of the interfacial ledges along the (100) interface also concurrently drives the rearrangement of the mismatch dislocations along the interface, for which the 8×7 and 6×5 CSL segments on the right side transform to the more favourable 7×6 CSL by climb and glide of the dislocation core upon the sweeping of the ledge. As shown in Fig. 3k, a new ledge (marked by arrow 3) enters from the left side into the field of view and repeats the same stop-and-go ledge flow with a dwell time ranging from 0.5 s to 1.5 s at the core of each dislocation (Fig. 3l). It can also be noted that the ledges are pinned for a longer period (2 s to 6 s) at the core of the mismatch dislocations along the $\text{Cu}_2\text{O}(110)/\text{Cu}(110)$ interface than that (0.5 s to 1.5 s) along the $\text{Cu}_2\text{O}(100)/\text{Cu}(100)$ interface. This indicates that the dwell time depends on the height of the interfacial ledges, where the ledges along the (110) interface are two-atom layers high, whereas the ledges along the (100) interface are monoatomic layer high. Meanwhile, the sweeping velocity of the ledge motion along the $\text{Cu}_2\text{O}/\text{Cu}$ interface can be calculated using the dwell time at the dislocation core and the distance between adjacent dislocations, which are 1.28 nm s^{-1} and 0.43 nm s^{-1} , respectively, for the (100) and (110) interfaces (Supplementary Text 6). The microscopic sweeping velocity of the ledge motion can be translated into the thickening rate of the underlying Cu layer, which can be measured macroscopically (Supplementary Text 6 and Supplementary Fig. 6).

H_2 can easily react with lattice O at the Cu_2O surface to form H_2O molecules. Accompanying the surface desorption of H_2O molecules is the concomitant formation of O vacancies at the oxide surface, as seen by the observed surface decay in Fig. 2a–d (Supplementary Text 4). Surface O vacancies can readily migrate towards the $\text{Cu}_2\text{O}/\text{Cu}$ interface

owing to the counter diffusion of lattice O from the $\text{Cu}_2\text{O}/\text{Cu}$ interface with low energy barriers (Supplementary Text 7 and Extended Data Fig. 1). Therefore, the ledge-flow speed may be related to degrees of easiness to remove lattice O in front of the $\text{Cu}_2\text{O}/\text{Cu}$ interfacial ledge. One would expect that O atoms that surround the dislocation core are more prone to departure owing to the lattice distortions around the core. Indeed, our DFT and nudged-elastic-band (NEB) calculations show that the O-vacancy formation energy and O diffusion barriers decrease as the ledge moves to the dislocation core (Extended Data Figs. 1 and 2, and Supplementary Text 7). This implies a more rapid $\text{Cu}_2\text{O} \rightarrow \text{Cu}$ transformation at these defect sites. However, on the contrary, our in situ TEM observations (Fig. 3) show that the $\text{Cu}_2\text{O} \rightarrow \text{Cu}$ transformation is actually impeded by the core of the mismatch dislocations, which thereby points to the effect from the supply of Cu atoms on the interfacial growth of Cu upon the departure of lattice O.

DFT calculations are further used to elucidate the ledge-flow growth of Cu using the (7×6) $\text{Cu}_2\text{O}/\text{Cu}$ interface configuration. Upon the sequential removal of lattice O in front of the interfacial ledge, neighbouring Cu atoms undergo spontaneous lateral relaxation towards the O-vacancy sites (as indicated by the black arrows in Fig. 4a), resulting in their perfect matching with the underlying Cu lattice. As seen from the DFT-optimized structure (Fig. 4b), the cyan Cu atom above the dislocation core shifts towards the right side by one atomic spacing to match the underlying Cu lattice. In turn, the mismatch dislocation line shifts from a red dashed 'T' to a pink solid 'T', consistent with the in situ HRTEM observations that show the $(8 \times 7) \rightarrow (7 \times 6)$ transformation in the CSL matching in front of the interfacial ledge (Fig. 3b,c). Another revealing feature noted in the DFT relaxed structure (Fig. 4b) is related to the dislocation core region, where the lateral relaxations of Cu atoms towards the O-vacancy sites result in two Cu-vacancy columns in front of the interfacial ledge, as marked by the blue dashed circles in Fig. 4b. The presence of the Cu-vacancy columns in the interfacial ledge is also

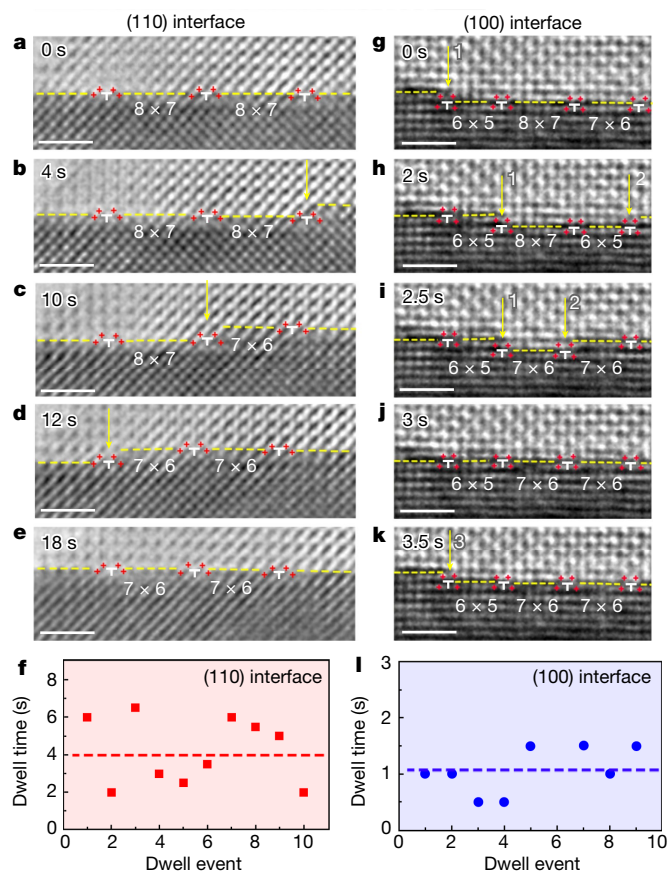


Fig. 3 | In situ atomic-scale observations of the interfacial ledge flow regulated by mismatch dislocations during the $\text{Cu}_2\text{O} \rightarrow \text{Cu}$ interfacial transformations at 623 K and 5.3 Pa of H_2 gas flow. **a–e**, Time-sequence HRTEM images (Supplementary Video 3) showing the regular interruption of the lateral flow of a double-atomic-height ledge along the $\text{Cu}_2\text{O}(110)/\text{Cu}(110)$ interface, where the ledge is pinned for about 2–6 s at the core of each dislocation and then resumes its lateral migration. **f**, Plot showing the dwell time of the interfacial ledges at the core of dislocations along the $\text{Cu}_2\text{O}(110)/\text{Cu}(110)$ interfaces. **g–k**, Time-sequence HRTEM images (Supplementary Video 4) showing the periodic pauses of monoatomic ledges at the core of the mismatch dislocations along the $\text{Cu}_2\text{O}(100)/\text{Cu}(100)$ interface, where the ledge is pinned for about 0.5–1.5 s at the dislocation cores and then resumes its lateral migration. The yellow arrows point to the location of the interfacial ledges. **l**, Plot of the dwell time of the interfacial ledges at the core of dislocations along the $\text{Cu}_2\text{O}(100)/\text{Cu}(100)$ interfaces. The yellow dashed lines mark the $\text{Cu}_2\text{O}/\text{Cu}$ interface and the yellow arrows point to the locations of the interfacial ledges. The core regions of the mismatch dislocations along the $\text{Cu}_2\text{O}/\text{Cu}$ interface in **a–e** and **g–k** are marked with white 'T's and red crosses. Scale bars, 1 nm (**a–e**, **g–k**).

confirmed by both HRTEM and HAADF imaging (the inset of Fig. 4b), showing the lower intensity of the atom columns within the ledge (Extended Data Figs. 3–6 and Supplementary Text 8). The formation of these Cu-vacancy columns is due to the decreased lattice spacings from Cu_2O to Cu and the (7×6) CSL interface configuration, in which the Cu_2O side has a smaller number of Cu atoms available to match the Cu side. The dislocation core is the preferred region to develop these Cu-vacancy columns owing to concentrated displacements of atoms in the core region (Fig. 1). By contrast, the interfacial Cu atoms located away from the dislocation core undergo spontaneously small displacements to match the Cu side upon the departure of interfacial lattice O, as seen in the DFT relaxed structure (Fig. 4b).

The pinned ledge flow at the core of mismatch dislocations is therefore attributed to the presence of Cu-vacancy columns in front

of the interfacial ledge. The ledge resumes its lateral flow only after the Cu-vacancy columns are completely filled with extra Cu atoms (Extended Data Fig. 5a,b). Therefore, the climb of the entire mismatch dislocation line to the new location of the $\text{Cu}_2\text{O}/\text{Cu}$ interface is essential before the sweeping of the dislocation core by the ledge flow. The resumed ledge propagation after the mismatch dislocation climb is like synchronized movements of atoms in front of the interfacial ledge, by which the interfacial ledge maintains a straight line between its two end points defined by the interface size of individual grains (Supplementary Text 9 and Extended Data Fig. 5c–e). As demonstrated in our DFT calculations shown in Fig. 4c, the mismatch dislocation is observed to climb by two atomic layers from the site marked with the pink dashed 'T' to the black solid 'T' site and the system energy decreases by $\Delta E = 0.44$ eV after the two vacancy columns are completely filled up with extra Cu atoms. This confirms the in situ TEM observations (Fig. 3a–e) that show the dislocation core climb by two atomic layers to the new $\text{Cu}_2\text{O}(110)/\text{Cu}(110)$ interface to accompany the sweeping of the dislocation core by the interfacial ledge. By contrast, the interfacial ledge along the $\text{Cu}_2\text{O}(100)/\text{Cu}(100)$ interface is only one-atomic-layer high (Fig. 3g–k), and thus the mismatch dislocation climbs by one atomic layer to the new $\text{Cu}_2\text{O}/\text{Cu}$ interface by filling up only one Cu-vacancy column above the dislocation core. Therefore, the ledge flow of the $\text{Cu}_2\text{O} \rightarrow \text{Cu}$ transformation at the (100) interface shows a shorter dwell time at the core of the dislocations compared with that along the (110) interface (Fig. 3f,l).

The climb of the mismatch dislocations requires the supply of extra Cu atoms either from the Cu_2O side or the Cu substrate side to join the formation of the extra Cu columns above the dislocation core. Our DFT and NEB computations show that extra Cu is supplied more favourably from the Cu side for the dislocation climb (Supplementary Text 10 and Extended Data Fig. 2). The dwelling of the interfacial ledge flow at the mismatch dislocations is induced by long-range diffusion of Cu from the Cu bulk to fill up the vacancies in the dislocation core. This corroborates well with our DFT calculations, which show the increasingly lowered system energy as the vacancies diffuse deeper into the Cu bulk and the higher energy barriers (0.57–0.64 eV) for the vacancy-assisted diffusion in the Cu bulk than the energy barriers (0.22–0.31 eV) for the interfacial jumps of metallic Cu atoms to the vacant sites of the dislocation core (Fig. 4d,e, Supplementary Text 11 and Extended Data Figs. 2 and 6). Edge dislocations in the Cu bulk can provide a convenient sink for vacancies diffusing away from the mismatch dislocations; conversely, Cu atoms are emitted by the recession of the extra half-plane of the edge dislocation and diffuse to the mismatch dislocation core, as schematically shown in Fig. 4f. This process is confirmed by the time-sequence HRTEM images in Fig. 4g (Extended Data Fig. 7), which show that edge dislocations in the Cu bulk act as a vacancy sink and experience the net positive climb in the Cu bulk. Similar stop-and-go $\text{Cu}_2\text{O} \rightarrow \text{Cu}$ interfacial transformation with the coordinated positive climb of edge dislocations in the Cu bulk is also observed for high-index $\text{Cu}_2\text{O}/\text{Cu}$ interfaces (Supplementary Text 12, Supplementary Video 6 and Extended Data Fig. 8). The long-distance diffusion required for the interfacial dislocation climb is further confirmed by our calculations using the classic dislocation model, which give the mismatch dislocation climb velocities of 0.067 nm s^{-1} for the (110) interface and 0.233 nm s^{-1} for the (100) interfaces, respectively (Supplementary Text 13 and Supplementary Fig. 7). These values agree well with our experimentally measured dislocation climb velocities of $\frac{d_{\text{Cu}(110)}}{t_{\text{dwell}(110)}} = \frac{0.2585 \text{ nm}}{4 \text{ s}} = 0.065 \text{ nm s}^{-1}$ for the (110) interface and $\frac{d_{\text{Cu}(100)}}{t_{\text{dwell}(100)}} = \frac{0.1828 \text{ nm}}{1 \text{ s}} = 0.183 \text{ nm s}^{-1}$ for the (100) interface (Fig. 3), respectively.

It should be borne in mind that the mismatch dislocations form an orthogonal network at the $\text{Cu}_2\text{O}/\text{Cu}$ interface, as illustrated schematically in Fig. 4h. In our in situ TEM experiments shown above, the $\text{Cu}_2\text{O}/\text{Cu}$ interfacial transformation is visualized along the direction parallel to the interfacial ledge. Clearly, the pinning effect on the interfacial transformation

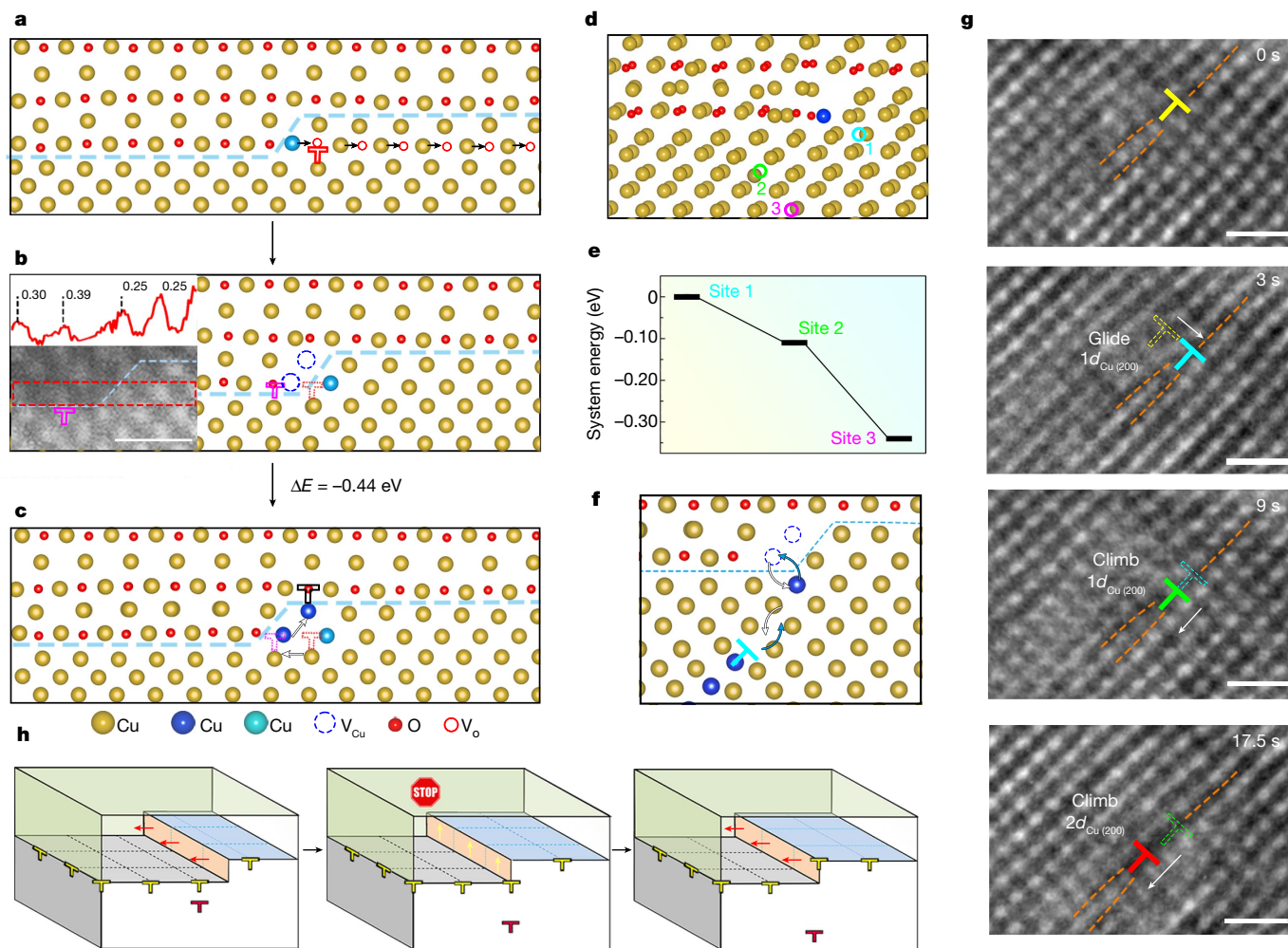


Fig. 4 | DFT modelling of the stop-and-go $\text{Cu}_2\text{O} \rightarrow \text{Cu}$ interfacial transformations. **a, b**, Upon sequential removal of the interfacial lattice O (red circles), adjacent Cu shifts spontaneously towards the vacated O, as indicated by the small black arrows in **a**, resulting in two Cu-vacancy columns (blue dashed circles in **b**). In turn, the dislocation glides to a pink solid 'T' from the original position (a red dashed 'T' in **b**). The inset in **b** is a HAADF-STEM image of the $\text{Cu}_2\text{O}/\text{Cu}(110)$ interface, showing the pinning of a double-atomic-height interfacial ledge at the dislocation core. The intensity profile along the red dashed rectangle shows relatively dimmed intensity of the ledge atom column owing to the presence of atomic vacancies. **c**, On filling up the two Cu-vacancy columns with extra Cu atoms (blue balls), the dislocation climbs spontaneously from pink dashed 'T' to the black solid 'T'. **d**, Evaluating the

system energy as a function of the distance of a Cu vacancy from the $\text{Cu}_2\text{O}/\text{Cu}$ interface by one (site 1), three (site 2) and five (site 3) atomic spacings in the Cu bulk. **e**, System energy plot as a function of the Cu-vacancy site shown in **d, f**. Schematic showing an edge dislocation in the Cu bulk acting as a source of Cu atoms to fill up the Cu vacancies for the mismatch dislocation climb in front of the interfacial ledge. **g**, Time-sequence HRTEM images (Supplementary Video 5) showing the glide and positive climb of an edge dislocation in the Cu bulk during the Cu_2O reduction. **h**, Schematic showing the stop-and-go transformation kinetics induced by the dislocation lines parallel to the interfacial ledge; the lateral flow of the interfacial ledge is pinned at the dislocation core until the dislocation line climbs to the upper terrace (Supplementary Video 7). Scale bars, 0.5 nm (inset in **b**, and **g**).

is associated with the climb of the dislocation lines parallel to the ledge (middle panel in Fig. 4h). The ledge-flow transformation is paused once the ledge encounters the dislocation lines. The interfacial ledge resumes its lateral propagation only after the entire dislocation line climbs to the new location of the $\text{Cu}_2\text{O}/\text{Cu}$ interface (right panel in Fig. 4h), which requires long-range diffusion of a large number of Cu atoms to fill up Cu vacancies along the entire dislocation line and therefore results in the observed dwelling of the interfacial ledge flow. By contrast, the other set of the dislocation arrays with their dislocation lines perpendicular to the interfacial ledge has a negligible contribution to the observed dwelling of the interfacial ledge. This is because those dislocation lines intersect with the ledge all the time (Fig. 4h) and their climb to the new $\text{Cu}_2\text{O}/\text{Cu}$ interface happens instantaneously by replenishing just one Cu atom for monoatomic ledges (along the $\text{Cu}_2\text{O}(100)/\text{Cu}(100)$ interface) or two Cu atoms for double-atomic-height ledges (along the $\text{Cu}_2\text{O}(110)/\text{Cu}(110)$ interface) (Supplementary Text 2 and Supplementary Fig. 4).

With in situ TEM imaging in-plane view, we further identify that the similar stop-and-go interfacial transformation can also occur along the other orthogonal direction, albeit not concurrently at the same place of the two perpendicular directions (Supplementary Text 14 and Extended Data Fig. 9). The non-coexistence of perpendicular interfacial ledges at the same place is because the ledges are the sink of O vacancies in the oxide (Fig. 4b and Extended Data Fig. 2), suggesting that an active zone of O-vacancy capture exists around an interfacial ledge and nucleating new ledges either parallel or perpendicular to the existing one in the close vicinity is unlikely. This corroborates well with our in situ TEM observations, which show that all the interfacial ledges are well separated without bunching during their motion. As shown by the observed climb motion of the mismatch dislocations at the $\text{Cu}_2\text{O}/\text{Cu}$ interface in conjunction with the positive climb of edge dislocations in the Cu bulk, the interfacial ledge along with its intersection with the mismatch dislocations serves first as a sink for O vacancies

produced originally at the oxide surface and then acts as the source for dumping the captured vacancies to the Cu side, thereby resulting in the eventual annihilation of the vacancies by edge dislocations in the Cu bulk (Fig. 4d–f).

The dynamic role of mismatch dislocations during boundary migration associated with solid-state transformations is a subject of general interest^{3,14,16}. As shown above, the mismatch dislocation array exerts intrinsic interface control of the transformation kinetics. Using metal oxidation as an example, the large crystal lattice changes accompanying the oxide growth typically lead to equilibrium mismatch dislocation spacings of about 1–3 nm. This high density of mismatch dislocations leads to the expected importance for interface control of the reaction kinetics at the metal/oxide interface. The interphase boundary containing terraces and ledges is a common feature for interface-mediated phase transformations^{1,17}. This is because introducing regular step risers that connect adjacent terraces can effectively increase the area of good matching, thereby minimizing the interfacial energy⁵. The retardation of global transformation kinetics by diffusion through the pinning action of intrinsic mismatch dislocations on the interfacial ledge flow was not yet known for inclusion in recent reviews of the role of interface structure in phase transformations^{1,3}. The pinning of a high density of interfacial ledges at the core of mismatch dislocations is also observed from the oxidation of bulk Cu (Extended Data Fig. 10) and at other heterophase interfaces^{26–28}, corroborating the broad universality of the stop-and-go interfacial transformation. For mismatch dislocations with both edge and screw components, the pinning of the interfacial ledges at the dislocation core depends on the climb velocity of the edge component and the cross-slip rate of the screw component to the new interface position, thereby restoring the mixed nature of the interfacial dislocations. Given the ubiquitousness of the ledge mechanism in solid–solid transformations^{1,3}, the important role of mismatch dislocations in mediating the solid-state reaction kinetics may be directly applicable to scaling reactions (that is, oxidation, nitridation, sulfidation and silicidation), precipitation reactions, solid-state displacement reactions and layer formation by interdiffusion, where the prototypes of basic processes governing the interfacial transformations exhibit similarities, including interfacial ledges, mismatch dislocations and vacancy-assisted diffusion.

Online content

Any methods, additional references, Nature Research reporting summaries, source data, extended data, supplementary information, acknowledgements, peer review information; details of author contributions and competing interests; and statements of data and code availability are available at <https://doi.org/10.1038/s41586-022-04880-1>.

1. Howe, J. M., Pond, R. C. & Hirth, J. P. The role of disconnections in phase transformations. *Prog. Mater. Sci.* **54**, 792–838 (2009).
2. Ikuhara, Y. & Pirouz, P. High resolution transmission electron microscopy studies of metal/ceramics interfaces. *Microsc. Res. Tech.* **40**, 206–241 (1998).
3. Hirth, J. P. & Mitchell, T. E. The role of interface structure in oxidation reactions. *Acta Mater.* **56**, 5701–5707 (2008).
4. Ernst, F. Metal–oxide interfaces. *Mat. Sci. Eng. R* **14**, 97–156 (1995).
5. Du Plessis, J. & Van der Merwe, J. On pointed minima in the interfacial energy of bicrystal systems. *Phil. Mag.* **11**, 43–51 (1965).
6. Pieraggi, B., Rapp, R. A., van Loo, F. J. J. & Hirth, J. P. Interfacial dynamics in diffusion-driven phase transformations. *Acta Metall. Mater.* **38**, 1781–1788 (1990).
7. Zou, L. F. et al. Dislocation nucleation facilitated by atomic segregation. *Nat. Mater.* **17**, 56–63 (2018).
8. LaGrow, A. P., Ward, M. R., Lloyd, D. C., Gai, P. L. & Boyes, E. D. Visualizing the Cu/Cu₂O interface transition in nanoparticles with environmental scanning transmission electron microscopy. *J. Am. Chem. Soc.* **139**, 179–185 (2017).
9. Zheng, H. M. et al. Multiferroic BaTiO₃–CoFe₂O₄ nanostructures. *Science* **303**, 661–663 (2004).
10. Wang, C. M., Thevuthasan, S., Gao, F., McCreedy, D. E. & Chambers, S. A. The characteristics of interface misfit dislocations for epitaxial α -Fe₂O₃ on α -Al₂O₃(0001). *Thin Solid Films* **414**, 31–38 (2002).
11. Stach, E., Schwarz, K., Hull, R., Ross, F. & Tromp, R. New mechanism for dislocation blocking in strained layer epitaxial growth. *Phys. Rev. Lett.* **84**, 947–950 (2000).
12. Müller, D. A. et al. The electronic structure at the atomic scale of ultrathin gate oxides. *Nature* **399**, 758–761 (1999).
13. Hull, D. & Bacon, D. J. *Introduction to Dislocations* (Butterworth-Heinemann, 2001).
14. Bollmann, W. *Crystal Defects and Crystalline Interfaces* (Springer-Verlag, 1970).
15. Li, L. Z., Xie, L. & Pan, X. Q. Real-time studies of ferroelectric domain switching: a review. *Rep. Prog. Phys.* **82**, 126502 (2019).
16. Hirth, J. P., Pieraggi, B. & Rapp, R. A. The role of interface dislocations and ledges as sources/sinks for point defects in scaling reactions. *Acta Metall. Mater.* **43**, 1065–1073 (1995).
17. Hirth, J. P. Ledges and dislocations in phase transformations. *Metall. Mater. Trans. A* **25**, 1885–1894 (1994).
18. Sinclair, R. & Mohamed, H. A. Lattice imaging study of a martensite-austenite interface. *Acta Metall.* **26**, 623–628 (1978).
19. McGibbon, A. J., Pennycook, S. J. & Angelo, J. E. Direct observation of dislocation core structures in CdTe/GaAs (001). *Science* **269**, 519–521 (1995).
20. Ross, F. M. & Minor, A. M. in *Springer Handbook of Microscopy* (eds Hawkes, P. W. & Spence, J. C. H.) 101–187 (Springer, 2019).
21. Stirman, J. N. & Crozier, P. A. Atomic-scale imaging of asymmetric Lomer dislocation cores at the Ge/Si(001) heterointerface. *Appl. Phys. Lett.* **84**, 2530–2532 (2004).
22. Gao, W. P., Sivaramakrishnan, S., Wen, J. G. & Zuo, J. M. Direct observation of interfacial Au atoms on TiO₂ in three dimensions. *Nano Lett.* **15**, 2548–2554 (2015).
23. Minor, A. M. et al. A new view of the onset of plasticity during the nanoindentation of aluminium. *Nat. Mater.* **5**, 697–702 (2006).
24. Oh, S. H. et al. In situ observation of dislocation nucleation and escape in a submicrometre aluminium single crystal. *Nat. Mater.* **8**, 95–100 (2009).
25. Kacher, J., Eftink, B. P. & Robertson, I. M. *Handbook of Mechanics of Materials* 1–37 (Springer, 2018).
26. Gutekunst, G., Mayer, J. & Rühle, M. The niobium/sapphire interface: structural studies by HREM. *Scr. Metall. Mater.* **31**, 1097–1102 (1994).
27. Sasaki, T. et al. Atomic and electronic structures of Ni/YSZ (111) interface. *Mater. Trans.* **45**, 2137–2143 (2004).
28. Mogck, S., Kooi, B. & De Hosson, J. T. M. Influence of metal–oxide interfaces on L₁₂ ordering in Cu₃Pd. *Acta Mater.* **52**, 4651–4658 (2004).

Publisher's note Springer Nature remains neutral with regard to jurisdictional claims in published maps and institutional affiliations.

© The Author(s), under exclusive licence to Springer Nature Limited 2022

Methods

Sample preparation

Cu(100) thin films with a nominal thickness of about 50 nm were deposited on NaCl(100) at 573 K using an ultrahigh-vacuum e-beam evaporation system. The Cu films were then removed from the substrate by dissolving sodium chloride in deionized water, and washed and mounted on a TEM specimen holder. Plasma cleaning of the specimen holder and specimens was performed before insertion in the environmental TEM.

In situ environmental TEM experiments

In situ environmental TEM experiments were conducted in a dedicated field-emission environmental TEM (FEI Titan 80–300) equipped with an objective-lens aberration corrector capable of delivering a spatial resolution of 0.08 nm at 300 kV and a gas manifold to control the pressure of various gases in the sample area^{29,30}. The procedure for the environmental TEM experiments is schematically shown in Supplementary Fig. 1 and includes the following steps. (1) As-loaded Cu films were deliberately annealed at about 873 K and about 0.13 Pa of H₂ gas flow to remove native oxide and generate tears and holes with faceted edges. These freshly created facets are oxide free and ideal for in situ TEM observations made in cross-sectional views of oxidation and reduction along the faceted edges (Supplementary Fig. 1). The cleanliness of the sample was confirmed by in situ electron diffraction and electron energy loss spectroscopy. (2) The specimen was then cooled to 623 K and H₂ gas was pumped out. The freshly cleaned Cu was oxidized at 623 K to form epitaxial Cu₂O islands along the edges of faceted holes in the Cu film by flowing O₂ gas at $p_{\text{O}_2} = 0.67$ Pa (Supplementary Fig. 1). (3) O₂ gas was then pumped out and the epitaxial Cu₂O on Cu was reduced to Cu in place at 623 K by flowing H₂ gas at a pressure of $p_{\text{H}_2} = 5.3$ Pa. (4) In situ HRTEM imaging was performed to visualize the Cu₂O → Cu interfacial transformations and the resulting dynamic motion of mismatch dislocations at $T = 623$ K and $p_{\text{H}_2} = 5.3$ Pa. In situ time-sequence HRTEM images were recorded along the Cu₂O(100)/Cu(100) and Cu₂O(110)/Cu(110) interfaces in an edge-on position.

Excluding the electron-beam effect

Potential TEM electron-beam irradiation effects on the observed stop-and-go interfacial transformations were evaluated carefully to ensure that the intrinsic behaviour of the interfacial transformations was studied. We performed comparison experiments by unblinking and blanking the electron beam. As shown in Fig. 2 (Supplementary Video 1), the electron beam was intentionally blanked for 60 s in the course of the in situ TEM observation, and no noticeable difference in the Cu₂O reduction rate was noted (in terms of the Cu₂O/Cu interface migration distance), confirming the negligible effect of the electron beam on the interfacial transformations. Conducting such comparative TEM observations to understand the effect of electron irradiation is part of the experimental protocol and in this case ensures that the electron-beam effect has a negligible effect on the interfacial transformation, and the stop-and-go flow of interfacial ledges that we see is inherent.

STEM experiments

HAADF imaging was conducted with probe-corrected STEM (Titan Themis G2 200). The microscope provides sub-ångström imaging of the core region of mismatch dislocations along the Cu₂O/Cu interface.

HRTEM and HAADF-STEM image simulations

DFT-optimized Cu₂O/Cu interfacial configurations were used for HRTEM and STEM simulations. HRTEM image simulations were performed using the multi-slice method with the parameters carefully matched to the experimental conditions (accelerating voltage, 300 keV; spherical aberration, 0.001 mm; defocus, −8 nm to 8 nm; thickness, 5–50 nm). HAADF-STEM image simulations were performed using the PRISM algorithm with parameters carefully matched to the

experimental conditions (accelerating voltage, 200 keV; probe semi-angle, 10 mrad; probe step, 0.1 Å).

Geometrical phase analysis

GPA³¹ of the HRTEM images was performed to identify the core region of mismatch dislocations along Cu₂O/Cu interfaces and quantify strain distribution around the dislocation core based on the atomic position displacements that use the bulk Cu lattice as the reference. The HRTEM images were filtered using the Wiener filter code with a noise-to-signal ratio of 0.2 to reduce the noise levels before conducting GPA.

Ab initio calculations

The total energy calculations were carried out within DFT^{32,33} using the plane-wave pseudopotential method³⁴ embodied in the Vienna Ab initio Simulation Package (VASP) code with ultra-soft pseudopotentials³⁵. Perdew–Burke–Ernzerhof (PBE) generalized gradient approximation³⁶ and projector augmented-wave³⁷ potential were performed to describe the electron–electron exchange and core–electron potential separately. The plane-wave cut-off energy was set to 400 eV, and a k -point sampling of $4 \times 2 \times 1$ based on the Monkhorst–Pack grids was used for the interface model. In modelling the Cu/Cu₂O interface, we used periodically repeated eight-layer slabs with their top and bottom layers fixed. We used the CSL structure of the 7×6 interface configuration, in which 6 Cu spacings in Cu₂O match 7 Cu spacings in the Cu substrate, resulting in a minimum strain of 0.226%. Considering the strong correlation effect among Cu $3d$ electrons, DFT+ U is employed in our simulations, where U represents the Coulomb interaction potential. According to a previous study³⁸, the values of 7.5 eV and 0.98 eV are adopted for the two Coulombic parameters U and J , respectively. All our calculations are spin-averaged, except for isolated molecular and atomic oxygen. The calculation of vacancy formation energies is defined as

$$E_f = E_{\text{slab}/\text{vac}} + E_{\text{atom}} - E_{\text{slab}},$$

where E_f is the vacancy formation energy, $E_{\text{slab}/\text{vac}}$ is the free energy of the slab with one vacancy, E_{atom} is the free energy of one single atom in the pure substance, and E_{slab} is the free energy of the slab without the vacancy. All the atomic structures are visualized using the Visualization for Electronic and Structure Analysis (VESTA).

Data availability

All data generated or analysed during this study are included in the published article and its Supplementary Information files.

- Sun, X. H. et al. Surface-reaction induced structural oscillations in the subsurface. *Nat. Commun.* **11**, 305 (2020).
- Sun, X. H. et al. Atomic-scale mechanism of unidirectional oxide growth. *Adv. Funct. Mater.* **30**, 1906504 (2020).
- Hýtch, M. J., Snoeck, E. & Kilaas, R. Quantitative measurement of displacement and strain fields from HREM micrographs. *Ultramicroscopy* **74**, 131–146 (1998).
- Kohn, W. & Sham, L. J. Self-consistent equations including exchange and correlation effects. *Phys. Rev.* **140**, A1133–A1138 (1965).
- Payne, M. C., Teter, M. P., Allan, D. C., Arias, T. & Joannopoulos, A. J. Iterative minimization techniques for ab initio total-energy calculations: molecular dynamics and conjugate gradients. *Rev. Mod. Phys.* **64**, 1045–1097 (1992).
- Kresse, G. & Furthmüller, J. Efficient iterative schemes for ab initio total-energy calculations using a plane-wave basis set. *Phys. Rev. B* **54**, 11169–11186 (1996).
- Vanderbilt, D. Soft self-consistent pseudopotentials in a generalized eigenvalue formalism. *Phys. Rev. B* **41**, 7892–7895 (1990).
- Perdew, J. P., Burke, K. & Ernzerhof, M. Generalized gradient approximation made simple. *Phys. Rev. Lett.* **77**, 3865–3868 (1996).
- Kresse, G. & Joubert, D. From ultrasoft pseudopotentials to the projector augmented-wave method. *Phys. Rev. B* **59**, 1758–1775 (1999).
- Anisimov, V. I., Zaanen, J. & Andersen, O. K. Band theory and Mott insulators: Hubbard U instead of Stoner I . *Phys. Rev. B* **44**, 943–954 (1991).

Acknowledgements This work was supported by the US Department of Energy, Office of Basic Energy Sciences, Division of Materials Sciences and Engineering under award number

DE-SC0001135. This research used the resources of the Center for Functional Nanomaterials and the Scientific Data and Computing Center, a component of the Computational Science Initiative, at Brookhaven National Laboratory which is supported by the US Department of Energy, Office of Basic Energy Sciences, under contract number DE-SC0012704. This work also used the computational resources from the Extreme Science and Engineering Discovery Environment (XSEDE) through allocation TG-DMR110009, which is supported by National Science Foundation grant number OCI-1053575. This research used the resources of the Environmental TEM Catalysis Consortium (ECC) as well, which is supported by the University of Pittsburgh and Hitachi High Technologies.

Author contributions G.Z. conceived the experiments and supervised the project. X.S., L.Z., S.D.H. and X.C. conducted experiments. D.W. conducted DFT calculations. M.L. developed the

codes for TEM image alignment. D.N.Z. and J.C.Y. contributed the experimental platform. X.S. and G.Z. analysed data and wrote the paper. All the authors commented on the manuscript.

Competing interests The authors declare no competing interests.

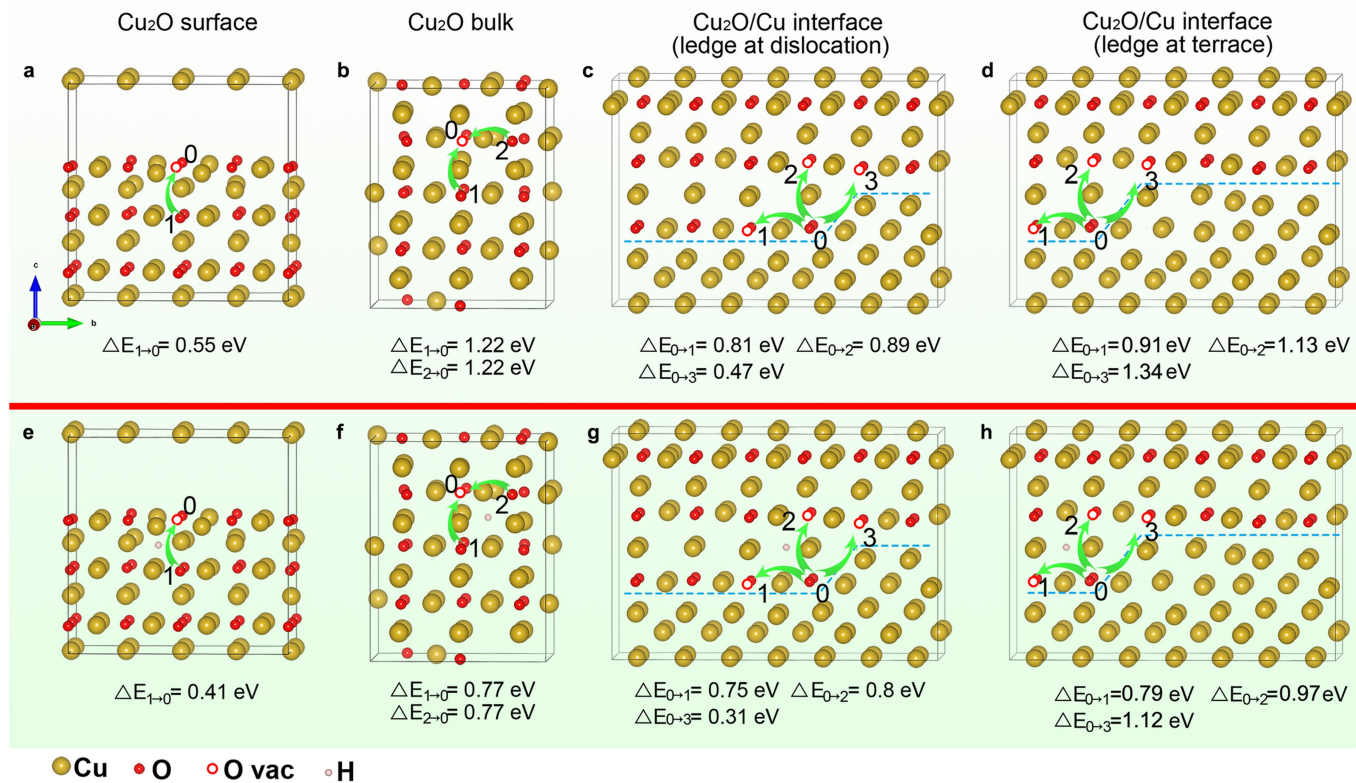
Additional information

Supplementary information The online version contains supplementary material available at <https://doi.org/10.1038/s41586-022-04880-1>.

Correspondence and requests for materials should be addressed to Guangwen Zhou.

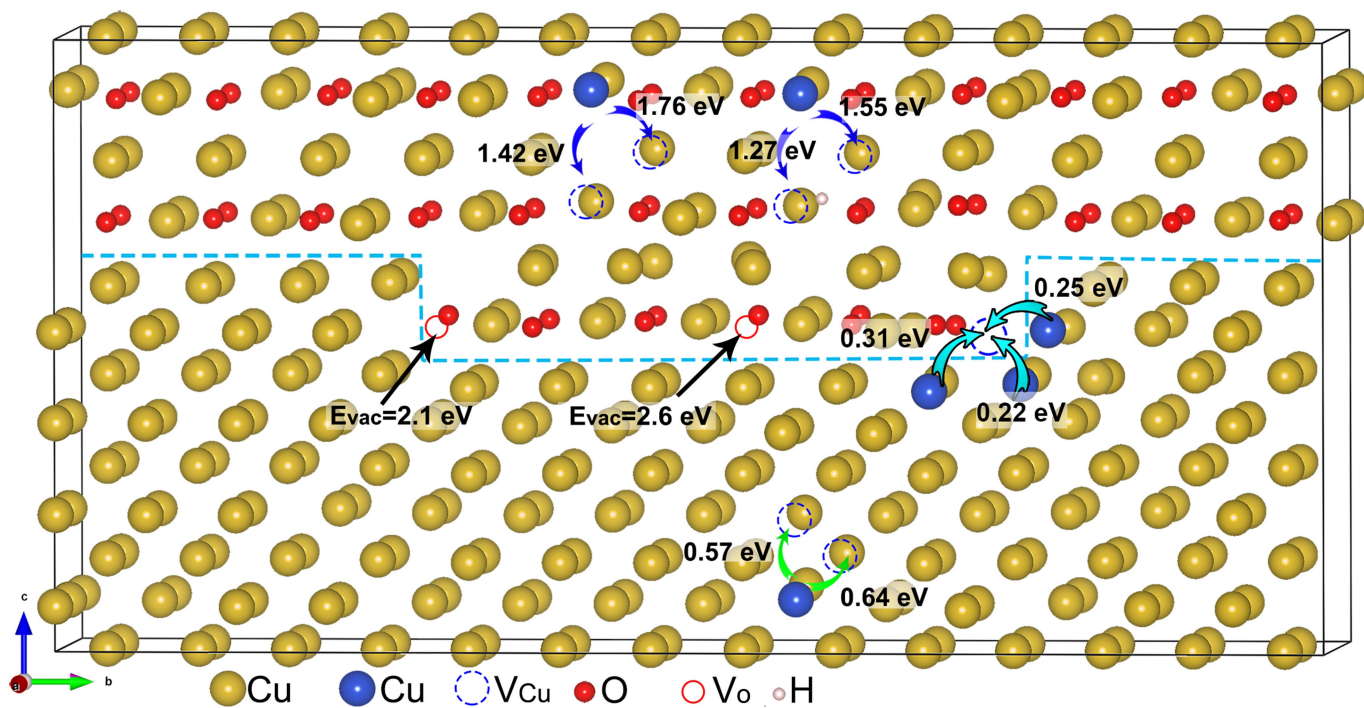
Peer review information *Nature* thanks Joshua Kacher and the other, anonymous, reviewer(s) for their contribution to the peer review of this work. Peer reviewer reports are available.

Reprints and permissions information is available at <http://www.nature.com/reprints>.



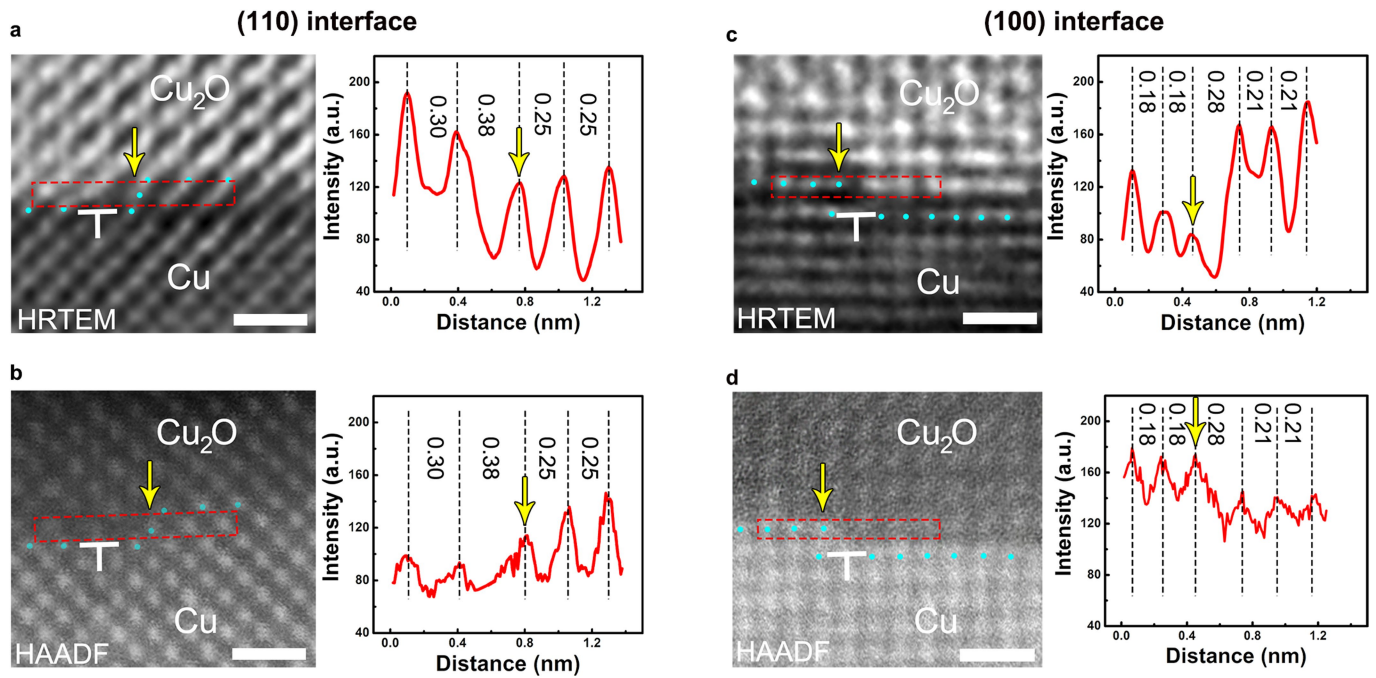
Extended Data Fig. 1 | NEB calculations of energy barriers for vacancy-assisted diffusion of O atoms with the absence (upper panel) and presence (lower panel) of interstitial H in Cu₂O. a, Surface/subsurface: migration of an O atom in the second layer to a vacant lattice site in the topmost layer. **b,** Bulk: interlayer (1→0) and intralayer (2→0) O-vacancy exchanges. **c,** Cu₂O/Cu interfacial ledge pinned at the mismatch dislocation core: migration of the O

atom at the mismatch dislocation core to its adjacent, non-equivalent vacant lattice sites. **d,** Cu₂O/Cu interface ledge away from the dislocation core by two Cu lattice spacings: migration of the O atom in front of the ledge to its adjacent, non-equivalent vacant lattice sites. **e–h,** Vacancy-assisted O diffusion along the same pathways as **a–d** with the presence of interstitial H in the Cu₂O lattice.



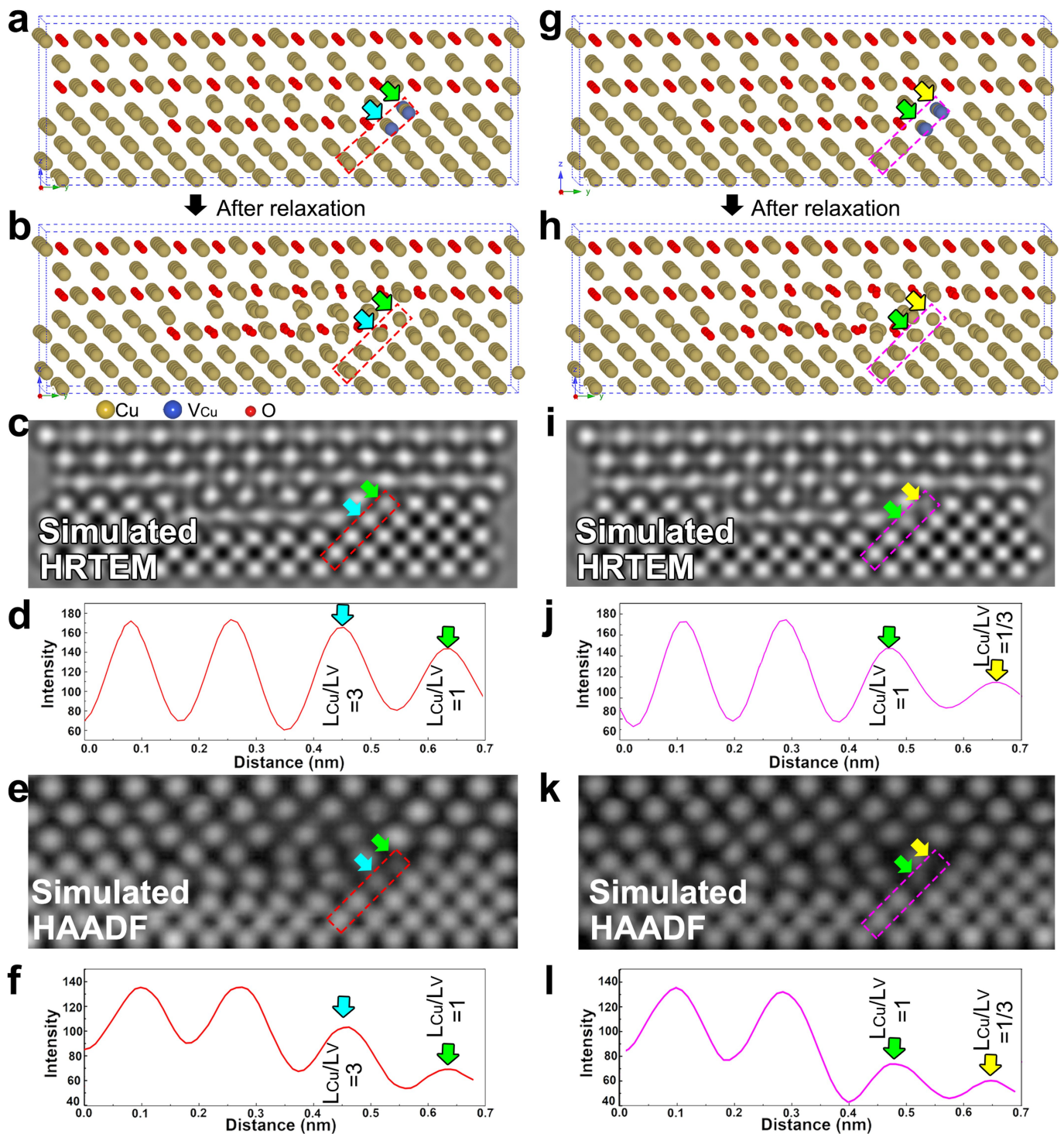
Extended Data Fig. 2 | DFT calculations of O-vacancy formation energies and Cu-vacancy exchange barriers. Black arrows mark the O-vacancy formation (and the associated energy) at the interfacial ledge (2.1 eV) and terrace (2.6 eV), respectively, indicating that the $\text{Cu}_2\text{O} \rightarrow \text{Cu}$ transformation occurs preferentially from the interfacial ledge, resulting in ledge flow. Blue arrows mark the interlayer Cu-vacancy exchange with and without the

interfacial H, respectively, along two non-equivalent pathways in Cu_2O . Green arrows mark atom-vacancy exchanges in the bulk of the Cu substrate. Cyan arrows mark the interfacial jumps of metallic Cu to the vacant site of the mismatch dislocation core in front of the interfacial ledge. Three non-equivalent types of atom-vacancy diffusion pathways are identified with the diffusion barriers in the range of 0.22 to 0.31 eV.



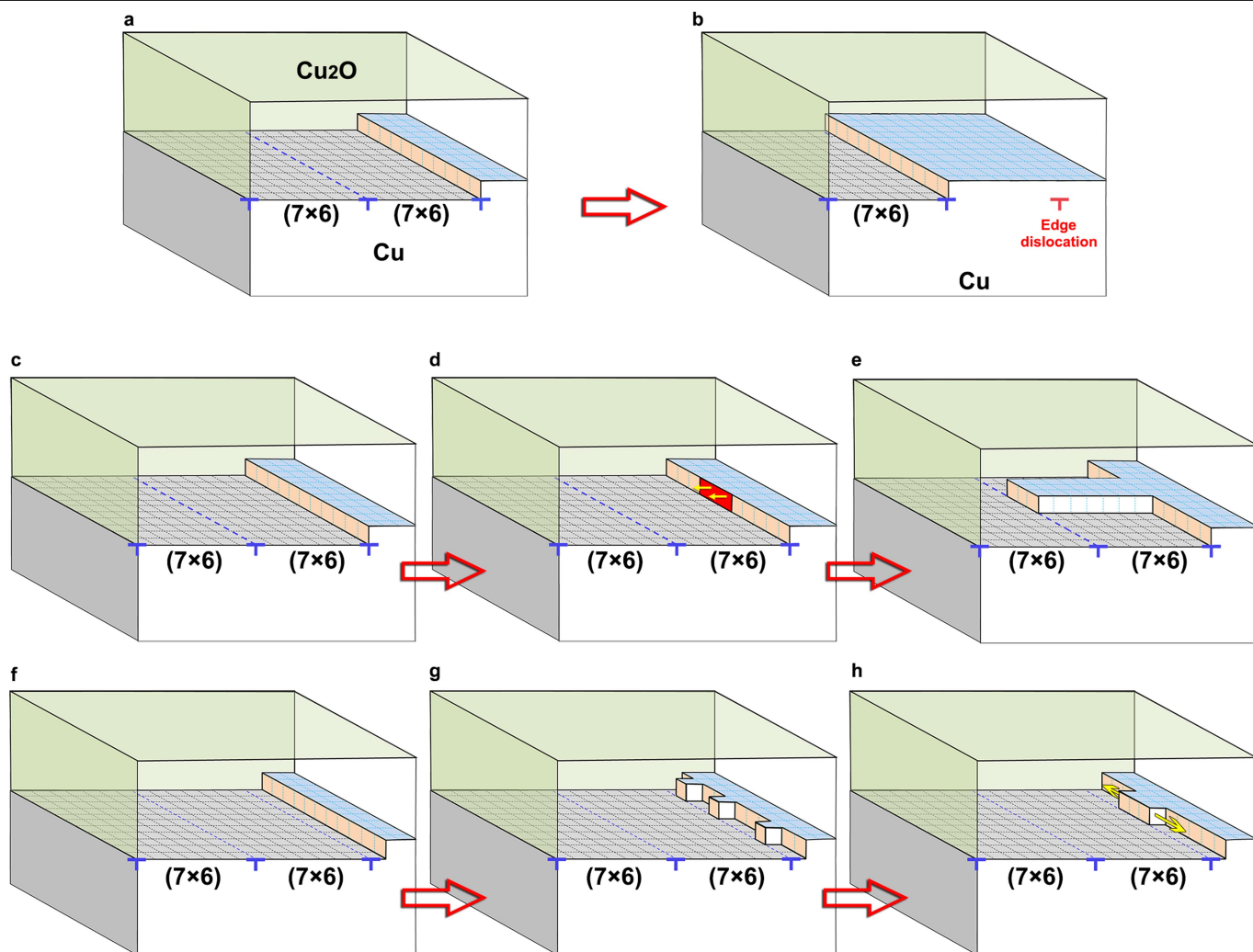
Extended Data Fig. 3 | HRTEM and STEM-HAADF imaging of Cu vacancies in interfacial ledges. **a, b**, HRTEM and HAADF images of the $\text{Cu}_2\text{O}(110)/\text{Cu}(110)$ interfaces showing the presence of a double-atomic-height interfacial ledge pinned at the mismatch dislocation core. **c, d**, HRTEM and HAADF images of the $\text{Cu}_2\text{O}(100)/\text{Cu}(100)$ interface showing a monoatomic interfacial ledge pinned at the mismatch dislocation. Shown on the right are the intensity profiles of the

$\text{Cu}_2\text{O}/\text{Cu}$ interface region marked by the red dashed rectangle in **a-d**. The yellow arrows mark the interfacial ledges. The relatively dimmed image contrast of the atom column of the interfacial ledges compared to the neighbouring interfacial terrace Cu atom columns indicates the presence of Cu vacancies within the interfacial ledge. Scale bar: 0.5 nm.



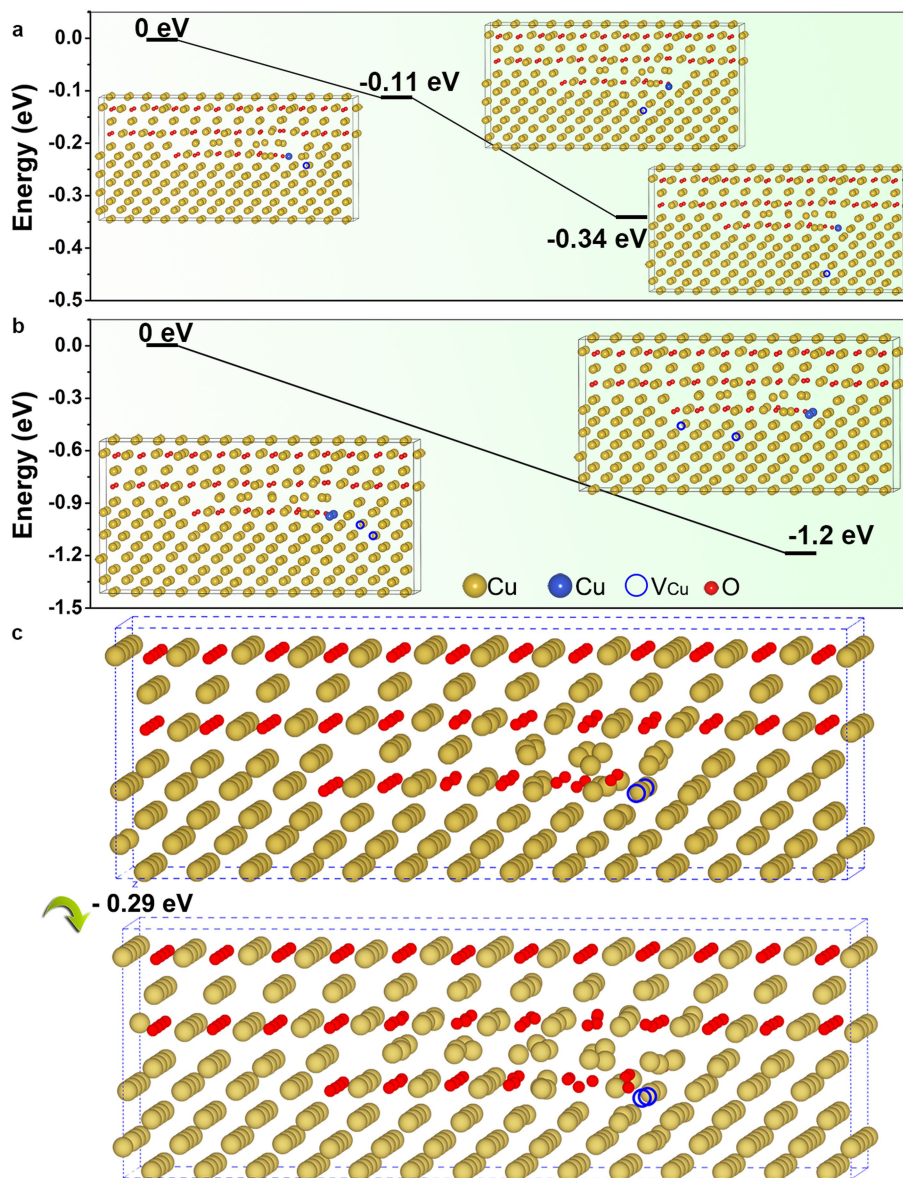
Extended Data Fig. 4 | HRTEM and HAADF simulations of interfacial ledges with different length ratios of the Cu and vacancy segments in the ledge. **a, b**, $\text{Cu}_2\text{O}(110)/\text{Cu}(110)$ interface model with $L_{\text{Cu}}/L_{\text{V}} = 3$ and 1 for the ledge atom columns marked by the cyan and green arrows, respectively, (L_{Cu} and L_{V} stand for, respectively, the lengths of the Cu and vacancy segments in the ledge) before **a** and after **b** DFT relaxation. **c, e**, Simulated HRTEM and HAADF-STEM images based on the DFT relaxed interface structure in **b, d, f**. Intensity profiles drawn from the red rectangles in **c** and **e**, respectively. **g, h**, $\text{Cu}_2\text{O}(110)/\text{Cu}(110)$

interface model with $L_{\text{Cu}}/L_{\text{V}} = 1$ and $1/3$ in the two ledge atom columns marked by the green and yellow arrows, respectively, before **g** and after **h** DFT relaxation. **i, k**, Simulated HRTEM and HAADF-STEM images based on the DFT relaxed interface in **h, j, l**. Intensity profiles drawn from the purple rectangles in **i** and **k**, respectively, showing the decreased image intensity with increasing the length of the vacancy segment, consistent with the experimental HRTEM and HAADF images in Extended Data Fig. 3.



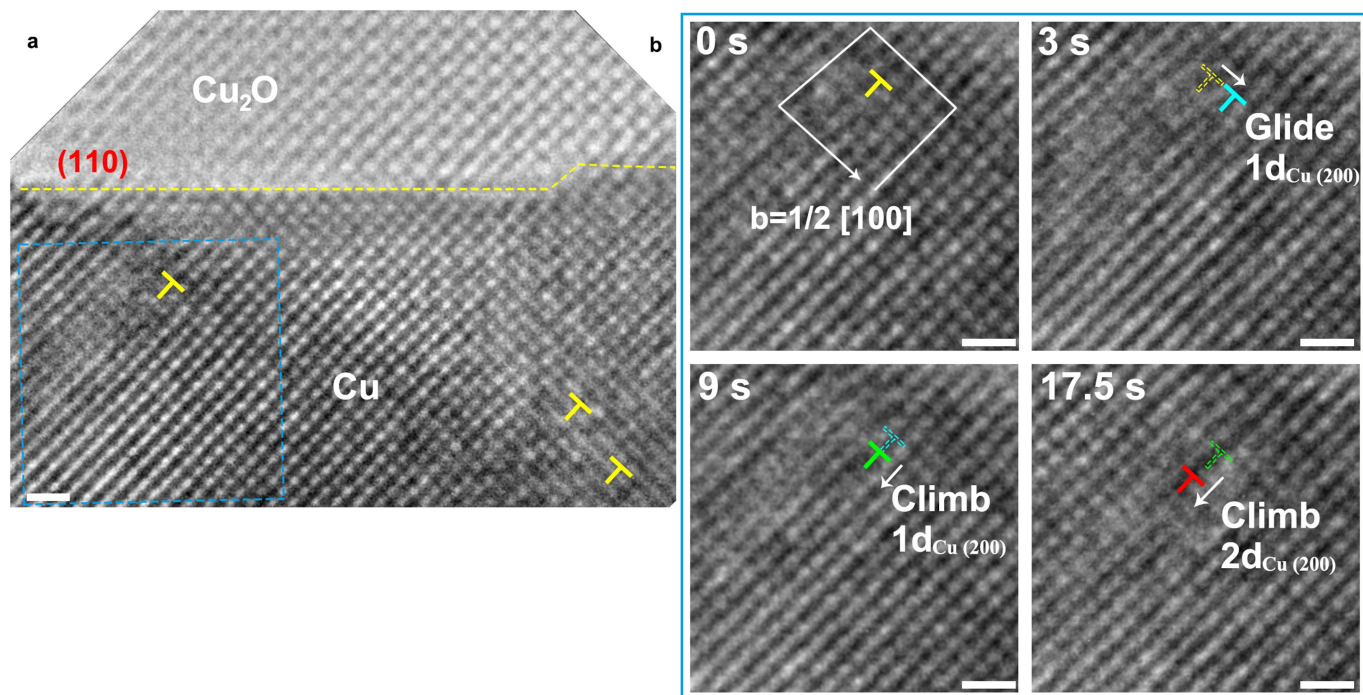
Extended Data Fig. 5 | Energetically unfavourable events of interfacial ledge propagation and possible pathways for filling the vacancy column of the interfacial ledge. a, b, Ledge flow without filling up the Cu-vacancy columns transforms the mismatch dislocation into an isolated edge dislocation in Cu. The mismatch dislocation (blue “T”) is buried by the newly formed Cu and becomes an isolated edge dislocation (red “T”), which will increase its energies due to the required presence of many broken bonds along the isolated dislocation line. By contrast, it is thermodynamically more favourable for the mismatch dislocations to climb to the new interface, by adsorbing extra Cu from the Cu substrate, to release some lattice mismatch strain upon the $\text{Cu}_2\text{O} \rightarrow \text{Cu}$ interfacial transformation. **c,** An initially straight ledge stops at a mismatch dislocation core. **d, e,** A segment of Cu vacancies (marked in red colour) in front of the interfacial ledge is filled up and the segment then

resumes its propagation to the next mismatch dislocation core (marked by the blue dashed lines). This is an unfavourable event because it will result in large geometric kinks with their side lengths of seven Cu lattice spacings for each propagation. Such an unsynchronized ledge flow leads to a highly kinked ledge with significantly increased ledge lengths and therefore is energetically unfavourable compared to the propagation of a straight ledge that happens only after all the Cu vacancies in front of the entire interfacial ledge are filled up. **f–h,** Two possible pathways of filling the vacancies in the interfacial ledge with Cu atoms supplied from the Cu bulk: **f, g,** randomly occupying the vacant sites, resulting in a high density of atomic kinks in the ledge; **g, h,** aggregation of Cu atoms into a one-dimensional (1D) segment of Cu, which subsequently grows along the ledge.



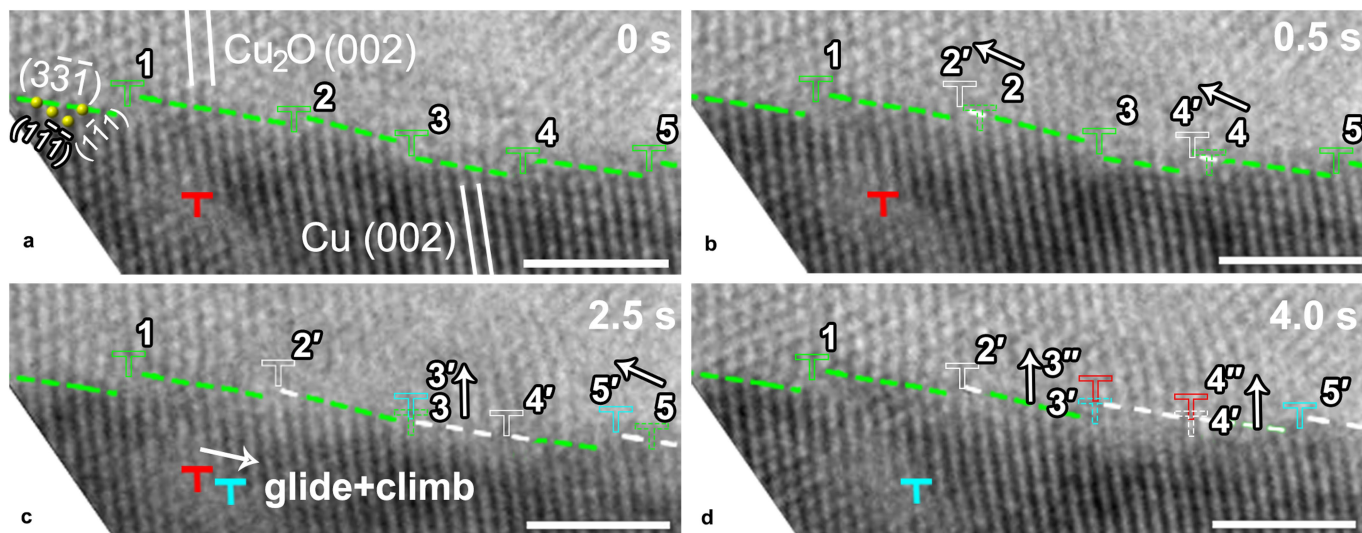
Extended Data Fig. 6 | Evaluation of the system energy changes as a function of the distance of Cu vacancies from the Cu₂O/Cu interface and of the aggregation of vacancies in the interfacial ledge. a, The swap of one Cu vacancy in the dislocation core with a Cu atom that is away from the Cu₂O/Cu interface by one, three and five atomic spacings in the Cu bulk, respectively. **b,** The swap of two Cu vacancies in the dislocation core with the Cu atoms that

have increased distance from the Cu₂O/Cu interface. **c,** Upper panel, Cu₂O/Cu interfacial ledge consisting of isolated vacancies and Cu atoms; lower panel, Cu₂O/Cu interfacial ledge consisting of 1D segments of aggregated Cu atoms and vacancies. The aggregation of vacancies (and Cu atoms) into 1D segments along the ledge lowers the system energy by 0.29 eV.



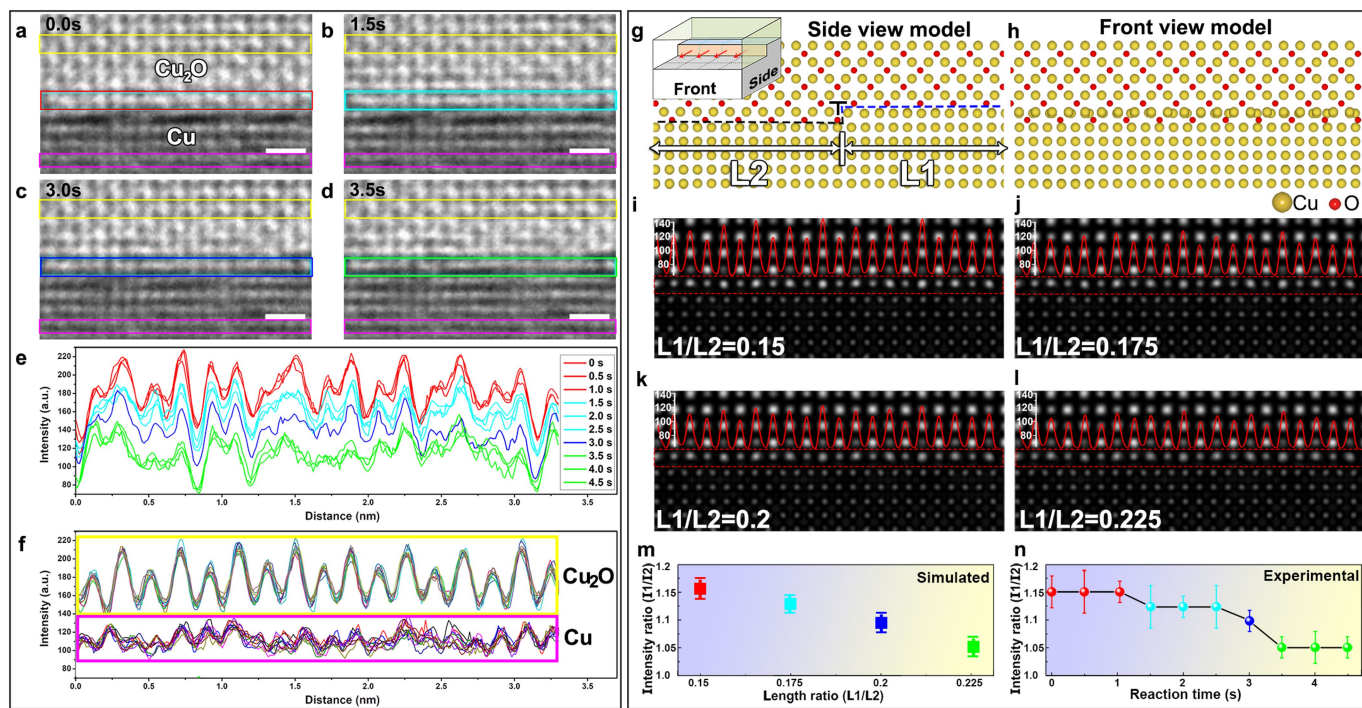
Extended Data Fig. 7 | In situ HRTEM observations of the positive climb motion of edge dislocations in the bulk of the Cu substrate during the stop-and-go $\text{Cu}_2\text{O} \rightarrow \text{Cu}$ transformation along the low-index $\text{Cu}_2\text{O}(110)/\text{Cu}(110)$ interface at 623 K and 5.3 Pa of H_2 gas flow. a, HRTEM micrograph showing the presence of edge dislocations (marked by yellow T) in the bulk of the Cu substrate. **b**, In situ HRTEM images (Supplementary Video 5) showing

the glide and positive climb of an edge dislocation in the region marked with the blue dashed square in **a**. The edge dislocation has a projected Burgers vector of $b = \frac{1}{2}[100]$ and is observed to glide (from yellow to cyan T positions) and climb (from cyan to red T positions) during the stop-and-go propagation of the interfacial ledges. Scale bar, 0.5 nm (**a, b**).



Extended Data Fig. 8 | In situ HRTEM observations of the stop-and-go $\text{Cu}_2\text{O} \rightarrow \text{Cu}$ transformation along a high-index $\text{Cu}_2\text{O}/\text{Cu}$ interface during the H_2 exposure at 623 K and 0.021 Pa of H_2 gas flow. a-d, Time-sequence HRTEM micrographs (Supplementary Video 6) showing the presence of a high density of interfacial ledges that are constantly pinned at the mismatch

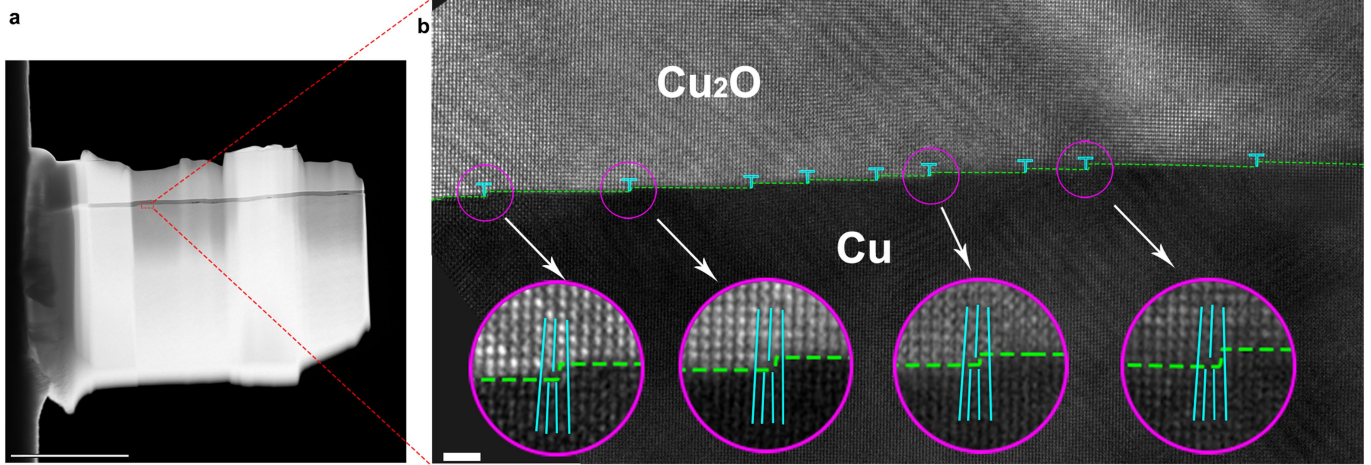
dislocations during the $\text{Cu}_2\text{O}/\text{Cu}$ interface propagation toward the Cu_2O side. The propagation of the interfacial ledges is accompanied by the glide and climb of the mismatch dislocation in front of the ledges. Meanwhile, an edge dislocation in the Cu bulk is observed to glide and climb deeper toward the Cu substrate during the $\text{Cu}_2\text{O} \rightarrow \text{Cu}$ interfacial transformation. Scale bar, 2 nm.



Extended Data Fig. 9 | (Left panel) In situ plan-view HRTEM imaging of the Cu₂O(100)/Cu(100) interfacial transformation at 623 K and 5.3 Pa of H₂ gas; (right panel) HRTEM simulation and intensity profile for the interfacial stop-and-go ledge flow along the e-beam direction.

a–d, Time-sequence HRTEM images (Supplementary Video 8) showing that the image contrast of the Cu₂O(100)/Cu(100) interfacial layer marked with red, cyan, blue and green rectangles becomes progressively dimmed in an intermittent manner. **e**, Time-sequence intensity profiles along the interface layer marked in **a–d**, showing intermittent attenuation in the image intensity of atomic columns in the interface layer. Similar intensity profiles are grouped in the same colour. **f**, Time-sequence intensity profiles showing the constant image contrast of the pure Cu₂O and Cu regions (marked by yellow and pink rectangles, respectively, in **a–d**). The intermittent attenuation of the image intensity within the Cu₂O(100)/Cu(100) interface layer reveals that the

Cu₂O→Cu interfacial transformation occurs also via the stop-and-go ledge flow along the fore-and-aft direction that is parallel to the e-beam direction of the TEM imaging. **g, h**, Side- and front-views of the Cu₂O(100)/Cu(100) interface model with the interfacial ledge pinning at the dislocation core. **i–l**, Simulated HRTEM images based on the front-view model (**h**), where the increased L1/L2 ratios correspond to the progressive Cu₂O→Cu transformation within the Cu₂O/Cu interface layer. The inset intensity profiles are extracted from the Cu₂O/Cu interface layer marked by red dashed rectangles in the simulated HRTEM images. **m**, Intensity ratios of high/low peaks of the intensity profiles of the Cu₂O/Cu interface of the simulated HRTEM images as a function of the L1/L2 ratio. **n**, Evolution of the intensity ratios of high/low peaks of the intensity profiles (**e**) of the Cu₂O/Cu interface of the experimental HRTEM images as a function of the reaction time. Scale bar, 0.5 nm (**a–d**).



Extended Data Fig. 10 | Pinning of interfacial ledges at the core of mismatch dislocations at a Cu₂O/Cu interface formed from the oxidation of bulk Cu.
a, SEM image of a TEM lamella prepared by focus ion beam (FIB) milling of a bulk Cu sample oxidized at 423 K for 10 min in air under the atmospheric pressure.

b, TEM image showing a high density of interfacial ledges that are pinned at the core of mismatch dislocations at the Cu₂O/Cu interface. Insets: HRTEM images of the core region of the mismatch dislocations along with the pinned ledge. Scale bar, 5 μm (**a**), 2 nm (**b**).